Deciphering the Origin of Interface-Induced High Li and Na Ion Conductivity in Nanocomposite Solid Electrolytes Using X-Ray Raman Spectroscopy

Laura M de Kort, Masoud Lazemi, Alessandro Longo, Valerio Gulino, Henrik P Rodenburg, Didier Blanchard, Christoph Sahle, Martin Sundermann, Hlynur Gretarsson, Ad M J van der Eerden, et al.

Deciphering the origin of interface-induced high Li- and Na- ion conductivity in nanocomposite solid electrolytes using X-ray Raman Spectroscopy

Laura M. de Kort,[a] Masoud Lazemi,[a] Alessandro Longo,[b,e] Valerio Gulino,[a] Henrik P. Rodenburg,[a] Didier Blanchard,[b] Christoph Sahle,[b] Martin Sundermann,[c,d] Hlynur Gretarsson,[c] Ad M.J. van der Eerden,[a] Hebatalla Elnaggar,[f] Frank M.F. de Groot,[a] and Peter Ngene[a*]

[a)] Materials Chemistry and Catalysis, Debye Institute for Nanomaterials Science, Utrecht University, Universiteitsweg 99, 3584 CG, Utrecht, The Netherlands

[b)] European Synchrotron Radiation Facility, Grenoble F-38000, France

[c)] Deutsches Elektronen-Synchrotron DESY, D-22607 Hamburg, Germany

[d)] Max Planck Institute for Chemical Physics of Solids, D-01187 Dresden, Germany

[e)] Istituto per lo Studio dei Materiali Nanostrutturati, Consiglio Nazionale delle Ricerche, Via Ugo La Malfa 153, 90146 Palermo, Italy

[f)] Institute of Mineralogy, Physics of Materials and Cosmochemistry, CNRS Sorbonne University, 4 Place Jussieu, Paris 75005, France

[*]Peter Ngene; Email: p.ngene@uu.nl

Abstract

Solid-state electrolytes (SSEs) with high ionic conductivities are crucial for safer and high-capacity batteries. Interface effects in nanocomposites of SSEs and insulators can lead to profound increases in conductivity. Understanding the composition of the interface is crucial for tuning the conductivity of composite solid electrolytes. Herein, X-ray Raman Scattering (XRS) spectroscopy is used for the first time to unravel the nature of the interface effects responsible for conductivity enhancements in nanocomposites of complex hydride-based electrolytes ($LiBH_4$, $NaBH_4$, $NaNH_2$) and oxides. XRS probe of the Li, Na, and B local environments reveals that the interface consists of highly distorted/defected and structurally distinct phase(s) compared to the original compounds. Interestingly, nanocomposites with higher concentrations of the interface compounds exhibit higher conductivities. Clear differences are observed in the interface composition of SiO_2- and Al_2O_3-based nanocomposites, attributed to differences in the reactivity of their surface groups. These results demonstrate that interfacial reactions play a dominant role in conductivity enhancement in composite solid electrolytes. Our work also showcases the potential of XRS in investigating interface interactions, providing valuable insights into the often complex ion conductor/insulator interfaces, especially for systems containing light elements such as Li, B, Na, and O, present in most SSEs and batteries.

Introduction

The potential of solid electrolytes, i.e., ion conductors, to improve battery safety significantly has led to enormous interest in replacing liquid organic-based battery electrolytes with ionic solids that possess high ionic conductivity at moderate temperatures.[1-10] Due to the intrinsic low ion mobility in solids compared to liquids (solutions), achieving high ion conductivity in solids at device-relevant (room) temperature has been of major interest. Among the different approaches to enhance ion conduction in solids, interface-induced high conductivity in heterogenous solid electrolytes or nanocomposites has raised serious scientific curiosity.[11-16] In these systems, a solid electrolyte forms a nanocomposite with a high surface area insulator, i.e., a non-ion conductor such as an oxide or ceramic.

The addition of the inert oxide nanoparticles can lead to an increase in the ionic conductivity by several orders of magnitude, and in most cases, without compromising, and sometimes even improving, other important properties of the electrolytes such as the electrochemical, mechanical, and interfacial stability. For instance, an enhancement in the room-temperature ionic conductivity by 4-5 orders of magnitude has been recently reported when complex hydrides, e.g., $LiBH_4$, $NaBH_4$, $Li_2B_{12}H_{12}$, $Li_2BH_4.NH_3$, $MgBH_4.NH_3$, and $CaBH_4.NH_3$ forms nanocomposites with oxides such as SiO_2, Al_2O_3, MgO, and ZrO_2.[10, 15, 17-21] Addition of nanoparticles of these oxides has also been shown to boost the interface and cycling stability of the composite solid electrolytes in all-solid-state Li-ion batteries.[13, 22-24]

The conductivity enhancement caused by the non-conducting secondary phase has been mainly attributed to electronic interactions leading to the formation of the so-called “space-charge region” at the interface between the two components.[25-27] This layer formation is caused by the electrochemical potential difference of the two compounds, which leads to a local ion redistribution. The discontinuity at the interface results in a deviation from local electroneutrality and, consequently, the formation of

a space-charge zone. Within this zone, the concentration of the charge-carrying defects is enriched, leading to enhancement in ionic conductivity.

Although the space charge model has often been used to explain the increased ionic conductivity in nanocomposite electrolytes, recent observations highlight a different phenomenon. Specifically, interface reactions can occur in several systems, particularly within metal hydride/oxide-based nanocomposites. This can lead to the formation of a defect-rich tertiary compound/phase at the interface between the two compounds.[18] Due to the highly defective nature of the interphase, the ionic conductivity can be several orders of magnitude higher than the starting compounds, thereby profoundly increasing the overall conductivity of the composite. The presence of such interphases will also undoubtedly modify the space charge layer. This could be the reason why the space-charge model has failed to quantitatively predict increased ion conductivity in several heterogeneous solid electrolytes.[13, 15]

Unraveling the nature and composition of such interphases is crucial for the rational design of highly conducting nanocomposite electrolytes. Regrettably, only a few studies have been reported on this topic to date. This is likely due to the complex nature of interphases. They are often amorphous with nanometric thickness and low concentrations, making their characterization challenging using most conventional techniques. In addition, it is non-trivial to use techniques that require an in-vacuo set-up, such as soft X-ray methods, e.g., X-ray photoelectron spectroscopy (XPS) and electron microscopy techniques. These challenges are particularly pronounced when working with metal hydride-based nanocomposite electrolytes, as they tend to decompose under high vacuum conditions.

In recent years, a few studies have been conducted to specifically investigate the interactions between the metal hydrides and the metal oxides using solid-state NMR, FT-IR, XPS, or Near Edge X-ray Absorption Fine Structures (NEXAFS).[28-34]Although each of these studies confirmed interface reaction between the metal hydride and the oxide, the nature of the interaction is still being debated. Taking $LiBH_4$/oxide nanocomposite as an example, some NMR studies suggest that the [BH_4^-] anion

near the interface remains intact, while other NMR studies indicate the formation of B-O, SiO-BH_3, Si-H, and Li-O bonds.[30, 31, 33, 34] For example, Dou *et al.*[29] suggested the formation of SiO-BH_3 structure, while Lambregts *et al.*[34] proposed a structure in which BH_4^- interacts with a Si site, as depicted in **Figure 1a**. The presence of B-O bonds has also been observed with XPS, FT-IR, and NEXAFS. However, these results are obscured due to possible air exposure during the measurements, the small penetration depth of the techniques, and the decomposition of $LiBH_4$ in high vacuum.[29, 31, 33] Thus, there is still no conclusive and well-resolved information available regarding the local interface structure.

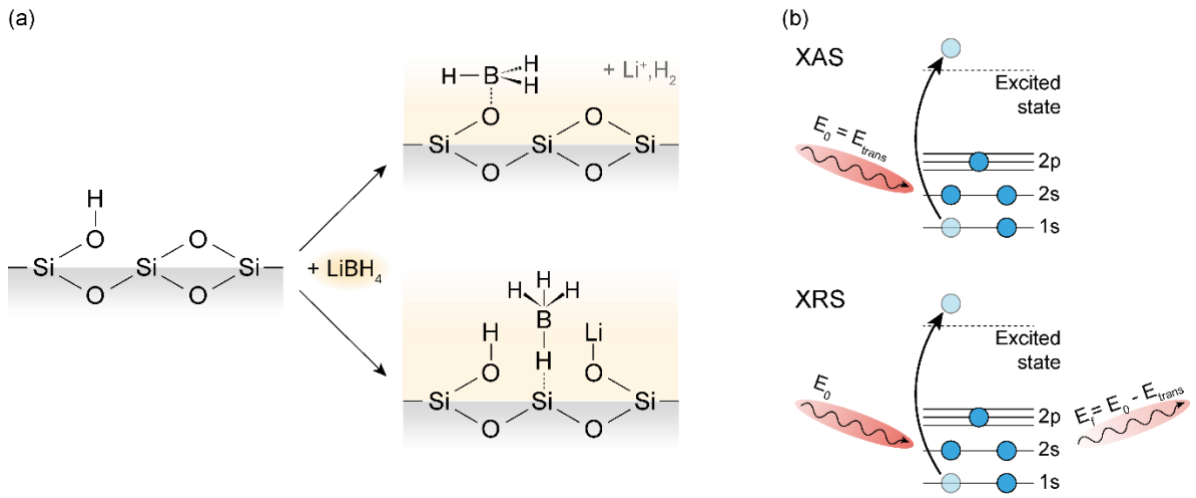

Figure 1 (a) Two-dimensional representation of the $LiBH_4$-SiO_2 interface structures proposed by Dou *et al.*[29] and Lambregts *et al.*[34] (b) A schematic representation of the X-ray Absorption and X-ray Raman Scattering process during an incident photon (with E_0) interacts with an atom in the ground state. This results in the excitation of a core electron and the case of XRS, an inelastically scattered photon (with E_f).

The limitations outlined above might be circumvented by utilizing a hard X-ray spectroscopic technique called X-ray Raman Scattering (XRS) spectroscopy, sometimes referred to as Non-resonant Inelastic X-ray Scattering (NIXS).[35] In this technique, a hard X-ray beam excites electronic transitions at soft X-ray absorption edges.[36, 37]By measuring the intensity of the scattered photons (into solid angle and energy window) as a function of the energy loss between the incident and the scattered X-ray energy, information similar to soft X-ray absorption spectroscopy (XAS) is obtained. This is schematically depicted in **Figure 1b**. Since XRS is an inelastic scattering technique, the scattering angle

can be used to enhance quadrupole excitations, like electron inelastic scattering, i.e., electron energy loss spectroscopy or EELS. In this way, the experimental advantages of hard X-ray techniques are retained, making XRS an ideal tool for obtaining chemical information of light elements with bulk sensitivity, even for nanocrystalline and amorphous samples contained in complicated sample environments.[38-43] In addition, it is possible to perform in-situ measurements,[38-44]as well as 3D tomography studies[38, 45, 46] by utilizing the imaging properties of XRS. Thus, XRS is a promising technique that could be applied to determine local structural environments in metal hydride/oxide nanocomposites for battery applications.

In this study, we explored XRS as a technique to study interface effects in nanocomposite solid electrolytes. Employing $LiBH_4$-, $NaBH_4$-, and $NaNH_2$/ metal oxide nanocomposites as archetypes, we investigated the chemical and structural transformations that occur in the local environments of Li, Na, and B upon nanocomposite formation. To this end, we prepared $LiBH_4$/oxide, $NaBH_4$/oxide, and $NaBH_4$/oxide nanocomposites with mesoporous SiO_2 and γ-Al_2O_3, the most widely used oxides for composite electrolytes. The use of the two different mesoporous oxide scaffolds enabled us to unravel the effects of the nature of the oxide on the interface reaction/interaction, i.e., the composition of the interface. Furthermore, we could uniquely probe the interface layer responsible for the high conductivities in nanocomposites with different metal hydride-metal oxide weight ratios. The B, Li, and Na local environments in this layer are immensely different compared to the pristine compounds. For example, near the interface between the metal hydride and SiO_2, boron from [BH_4^-] changes from tetrahedral coordination to a trigonal configuration. In addition, changes in the Li and Na environment indicate that Li^+ and Na^+ (from the metal hydrides) are greatly affected by interaction with the oxide, while an N-O-like bond is present for the $NaNH_2$-based nanocomposites. This work provides new insight into the interface interaction in metal hydride/oxide nanocomposites. Furthermore, it demonstrates that XRS is a promising technique to study light elements and amorphous materials.

Experimental methods

Samples and sample preparation

Several $LiBH_4$-, $NaBH_4$-, and $NaNH_2$/oxide nanocomposites were prepared by melt infiltration following the procedures described earlier.[18, 47] $LiBH_4$ (purity > 98%, Sigma-Aldrich) was mixed with mesoporous alumina (γ-Al_2O_3), silica (SBA-15), and grafted silica (M-SBA-15, with M = Al, Zr) and subsequently infiltrated by heating to 285 °C under hydrogen pressure. $NaBH_4$ (99.99%, Sigma-Aldrich) was mixed with mesoporous alumina (γ-Al_2O_3) and silica (MCM-41), and subsequently infiltrated by heating to 525 °C under hydrogen pressure. The amount of metal hydride confined in the oxide pores, i.e., the pore filling fraction (PF), was varied from 15% to 130% to probe the interface interaction specifically. In other words, the volume of $LiBH_4$ corresponds to 0.15 to 1.3 times the pore volume of the oxide. By excluding the contribution of bulk metal hydride to the XRS signal (via this approach), the interface interaction becomes more predominant at low concentrations of metal hydride in the nanocomposites. Reference compounds ($Li_2B_{12}H_{12}$, $LiBO_2$, H_3BO_3, $NaNO_3$, $NaNO_2$, $Na_2B_{12}H_{12}$, $B_{10}H_{14}$, B_2O_3, and $NaBO_2.4H_2O$) were purchased and used either without further treatment or after an evacuation and drying procedure prior to storage under inert atmosphere. All storage and handling of the chemicals and prepared nanocomposites was done in an argon-filled glovebox (H_2O and O_2 < 0.1 ppm).

Grafted silica (M-SBA-15, with M = Al, Zr) was prepared by drying 1.2 g SBA-15 in static air for 2 hours at 250 °C. The grafting reaction was performed under an N_2 atmosphere using a Schlenk line. The reaction mixture was prepared by dissolving the needed amount of precursor salt, either $Al(OC_3H_7)_3$ or $Zr(OC_3H_7)_4$, to obtain a Si/M ratio 10 in dry isopropanol. Subsequently, the dried silica scaffold was added, and the mixture was left to stir overnight. The resulting suspension was filtrated and washed with isopropanol. After a final drying (2 hours at 120 °C) and calcination procedure (4 hours at 500 °C, GHSV = 20 mL min^{-1} g^{-1} N_2/O_2 flow), the grafted silica was placed in an argon-filled glovebox.

General characterization

Diffuse reflectance infrared Fourier transform spectroscopy (DRIFTS) measurements were performed in a Perkin-Elmer 2000 spectrometer equipped with a liquid nitrogen-cooled MCT detector. Spectra were recorded between 4500 and 500 cm^{-1} with 4 cm^{-1} resolution, averaging over 16 scans and using anhydrous KBr as a background. The porosity of the mesoporous oxides was probed with nitrogen physisorption measurements performed on a Micromeritics Tristar 3000. Using the Brunauer, Emmett and Teller (BET) and Barrett, Joyner and Halenda (BJH) adsorption model theories, surface area and pore size distribution could be obtained.[48, 49] The specific surface area (A_{BET}) and total pore volume, as determined from the adsorbed quantity close to nitrogen saturation pressure ($p = p_0$) are summarized in **Table 1**.

Table 1. Nitrogen physisorption results of oxide scaffolds.

Oxide scaffold	BET area ($m^2 g^{-1}$)	Pore volume ($cm^3 g^{-1}$)	Average pore diameter (nm)
SiO_2 (SBA-15)	722	0.68	6.4
Al-SiO_2 (Al-SBA-15)	628	0.67	6.4
Zr-SiO_2 (Zr-SBA-15)	640	0.64	6.2
SiO_2 (MCM-41)	1071	1.11	2.7
γ-Al_2O_3	186	0.49	8.8

The conductivities of the $LiBH_4$/(grafted) SiO_2 nanocomposites were determined by measuring Electrochemical Impedance Spectroscopy (EIS) using a Princeton Applied Research Parstat 2273 potentiostat placed in a custom-made Büchi B-585 glass oven. Pellets (t = 0.5 – 1.0 mm, ø = 13 mm) were prepared by pressing (P = 150 MPa) about 80 – 150 mg between stainless-steel electrodes covered with lithium foil. The EIS measurements were performed by heating the samples from RT to 130 °C with increments of 10 °C.An EIS measurement was acquired at each increment with a 20 mV RMS modulated alternating current potential in a frequency range from 1 MHz to 1 Hz. The complex impedance spectra were fitted to a least squares minimum with a circuit consisting of a resistor (R) in

parallel with a constant phase element (CPE). Based on the obtained resistance value, the electrode area (A = 1.33 cm^2), and the thickness (t) of the pellet, the conductivity, σ, was calculated via σ = t/AR.

X-ray Raman Scattering experiments

Lithium (Li) and boron (B) 1s (K-edge) XRS spectra were collected at the ID20 beamline[50] of the European Synchrotron Radiation Facility (ESRF), Grenoble, France. An air-tight, ex-situ XRS cell developed by our group (**Figure 2**) was placed in a pre-mounted cell holder in a transmission configuration, so the cell was in the same position in every measurement. During the measurement, the cell was kept under a vacuum environment. Sodium (Na) and boron (B) K-edge XRS spectra were collected at the P01 beamline of the Deutsches Elektronen-Synchrotron (DESY) Petra III, in Hamburg, Germany. A slightly modified version of the air-tight, ex-situ XRS cell was mounted on a pre-constructed cell holder in a configuration with an incidence angle of 10°. Both at ESRF and at DESY, the samples were prepared in an argon-filled glovebox by compressing 10 – 40 mg into a pellet (ø = 10 mm). Subsequently, the compressed pellet was placed in the XRS cell between two Kapton foils (ESRF) or between a Kapton foil and a Kapton/aluminium foil (DESY). The aluminum provides rigidity to the Kapton foil and prevents beam damage, thereby preventing contamination of the samples by air and moisture during measurement.

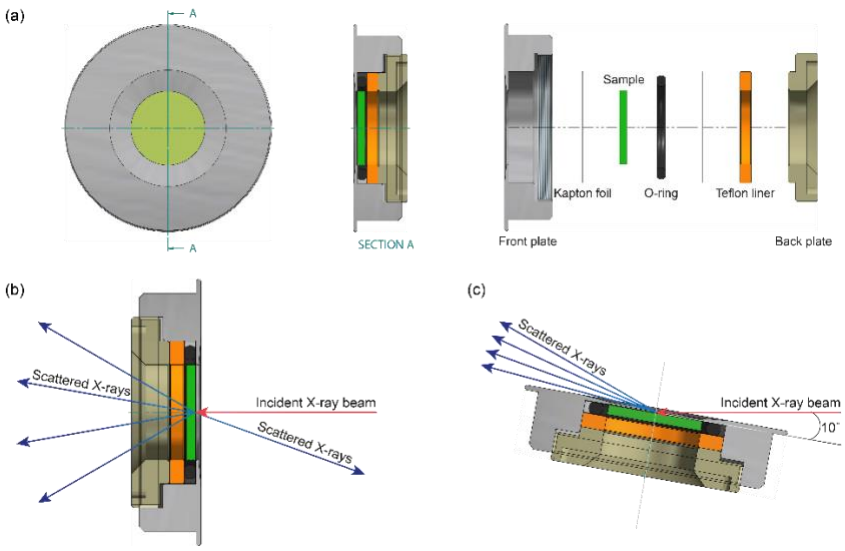

Figure 2. (a) Schematic representation of the air-tight cell used for ex-situ XRS measurements used in the (b) transmission and (c) grazing incidence configurations

The XRS scans were performed using the inverse energy scan technique in which the scattered photons are analyzed at a fixed energy, and the energy transfer is controlled by tuning the incident photon energy. About 3-10 scans were taken for a single measurement, depending on the quality of the signal from the measured edge. The incident photon energy was selected with a Si(311) monochromator. The XRS spectra were collected by scanning the incident beam energy relative to the fixed analyzer energy of 9690 eV with a resolution of 7 eV. At ESRF, the XRS spectra were collected using Medipix detectors (2D photon-counting X-ray detectors with a 55 µm spatial resolution) with an average q-vector of 4.1 to 4.9 $Å^{-1}$ (2θ = 50 - 60°). At DESY, the XRS spectra were collected using Medipix detectors with an average q-vector of 4.5 $Å^{-1}$ (2θ = 55°). The identification of the detector pixels that record scattering from the sample, or the regions of interest (ROIs), were defined manually. The scattering signals obtained from the selected ROIs were normalised to the f-sum rule[51] by background subtraction of parameterized Pearson VII functions guided by Hartree-Fock calculated core atomic profiles as described by Sahle *et al*. using the XRStools software package.[52] The final spectra are plotted as normalized scattered intensity versus energy loss. The spectra of the nanocomposites were smoothened by adjacent averaging over 5 points.

Li- and B- XRS spectra of high purity $LiBH_4$ (99% purity) were acquired to verify that the measurement cells are air-tight and that the samples are not exposed to air during sample preparation, transfer, and measurements. The spectrum of the high-purity sample did not show any peaks related to impurities or oxidized compounds, which confirms that our measurement cells are air-tight and protect the samples from air exposure during sample preparation, transfer, and measurement. Oxidation or beam-induced sample damage during the XRS measurement was monitored by comparing the initial scans of the measurement to subsequent scans. In this case, a slight decrease in the intensities of the peaks is observed. This indicates that while the samples did not oxidize during the measurement, the sample is affected by prolonged beam exposure. These changes are attributed to the low stability of borohydrides in the beam. To minimize beam damage, measurement durations

were reduced, and for extended measurements, the beam was repositioned across various areas of the sample at regular intervals during the measurement.

Results and discussion

X-ray Raman Scattering Analysis of $LiBH_4/SiO_2$ Nanocomposites

Our analysis starts with $LiBH_4/SiO_2$ nanocomposites, one of the most widely investigated hydride/oxide nanocomposite electrolytes. Li and B K-edges XRS spectra of pristine $LiBH_4$ and $LiBH_4/SiO_2$ with 130%, 50%, and 15% pore filling were measured **(Figure 3b-e and S1)**. In the $LiBH_4/SiO_2$ nanocomposite with 130% pore filling, the $LiBH_4$ volume is 1.3 times the total pore volume of the scaffold, ensuring complete filling of the scaffold pores. Moreover, additional $LiBH_4$ covers the outer surface of the oxide particles, establishing a conductive path for long-range Li-ion transport over the non-conducting oxide particles. The lower pore-filling fractions roughly correspond to a 1 nm (PF = 50%) and 0.3 nm layer (PF = 15%) of $LiBH_4$ covering the SiO_2 pore walls, assuming that $LiBH_4$ completely wets the silica surface. The composition of the nanocomposites is schematically illustrated in **Figure 3a**. Since the interface layer in $LiBH_4$/oxide nanocomposites is 1 – 2 nm,[16, 53, 54] the nanocomposites with ≤ 50% PF fractions will likely provide more specific information on the $LiBH_4$-SiO_2 interface.

The changes in the chemical structure of $LiBH_4$ upon nanocomposite formation in mesoporous SiO_2 are explored by comparing pristine $LiBH_4$ to the $LiBH_4/SiO_2$ nanocomposites. In the Li K-edge spectra of pristine $LiBH_4$ (**Figure 3b**, black line), a clear absorption peak is visible at 59.9 eV. This feature corresponds to the transition of the Li 1s core electron to unoccupied orbitals (with a p character), as has been reported for many lithium salts such as lithium halides and lithium borates.[55-58] The B K-edge spectra of pristine $LiBH_4$ show three characteristic features (**Figure 3c**, black line) as follows:

I. An edge peak is observed at 191.5 eV, which is associated with the transition of a B 1s electron from the tetrahedral $[BH_4]^-$ anion to an unoccupied boron antibonding $2a_1$ orbital (**Figure 4a**).[59]

II. A small peak can be observed at 193.8 eV, which is attributed to the transition of B 1s electrons to unoccupied a'' orbitals in planar system[59-63] (**Figure 4b**), such as BF_3, BH_3 or trigonal B-O from $LiBO_2$ or B_2O_3 impurities commonly found in commercially available $LiBH_4$.

III. The broadband between 195 and 205 eV is related to the transition of a B 1s electron to an unoccupied $2t_2$ orbital of tetrahedral boron.[59-62] Note that this broadband sometimes contributes to trigonal boron, as it also exhibits a transition to unoccupied orbitals (generally e') in this region.[59-62] These results are in line with previous XRS results reported by our group.[39, 40]

Expectedly, clear differences exist between the spectra of pristine $LiBH_4$ and those of the nanocomposites. Firstly, in the Li K-edge spectrum (**Figure 3b**) of the $LiBH_4/SiO_2$ nanocomposites with 130% PF, the peak at 59.9 eV has become less intense compared to pristine $LiBH_4$. Secondly, a broad feature is observed around 64 eV. The intensity of the peak at 59.9 eV decreases with lower pore filling, and a shoulder appears at 55.6 eV. Thirdly, the region between 62 eV and 75 eV starts to show several features. The reduced intensity of the peak at 59.9 eV, combined with the formation of a shoulder, demonstrates that the unoccupied orbitals of Li^+ become progressively filled and the bond between the anion and Li^+ becomes more covalent, for example, due to the presence of a less electronegative anion, or Li^+ becoming more metallic.[40, 56, 57] The features in the fingerprint region between 62 eV and 75 eV might be due to multiple scattering resonances or the presence of lithium compounds with stronger ionic bonds, such as Li_2O.[57, 64, 65] Overall, these results suggest that near the SiO_2 surface, two different lithium compounds are present, one in which Li^+ is weakly bonded to the complex anion (e.g. BH_3 or highly distorted BH_4), and one in which Li is closely bonded to O, such as in Li-O, or Si-O-Li.

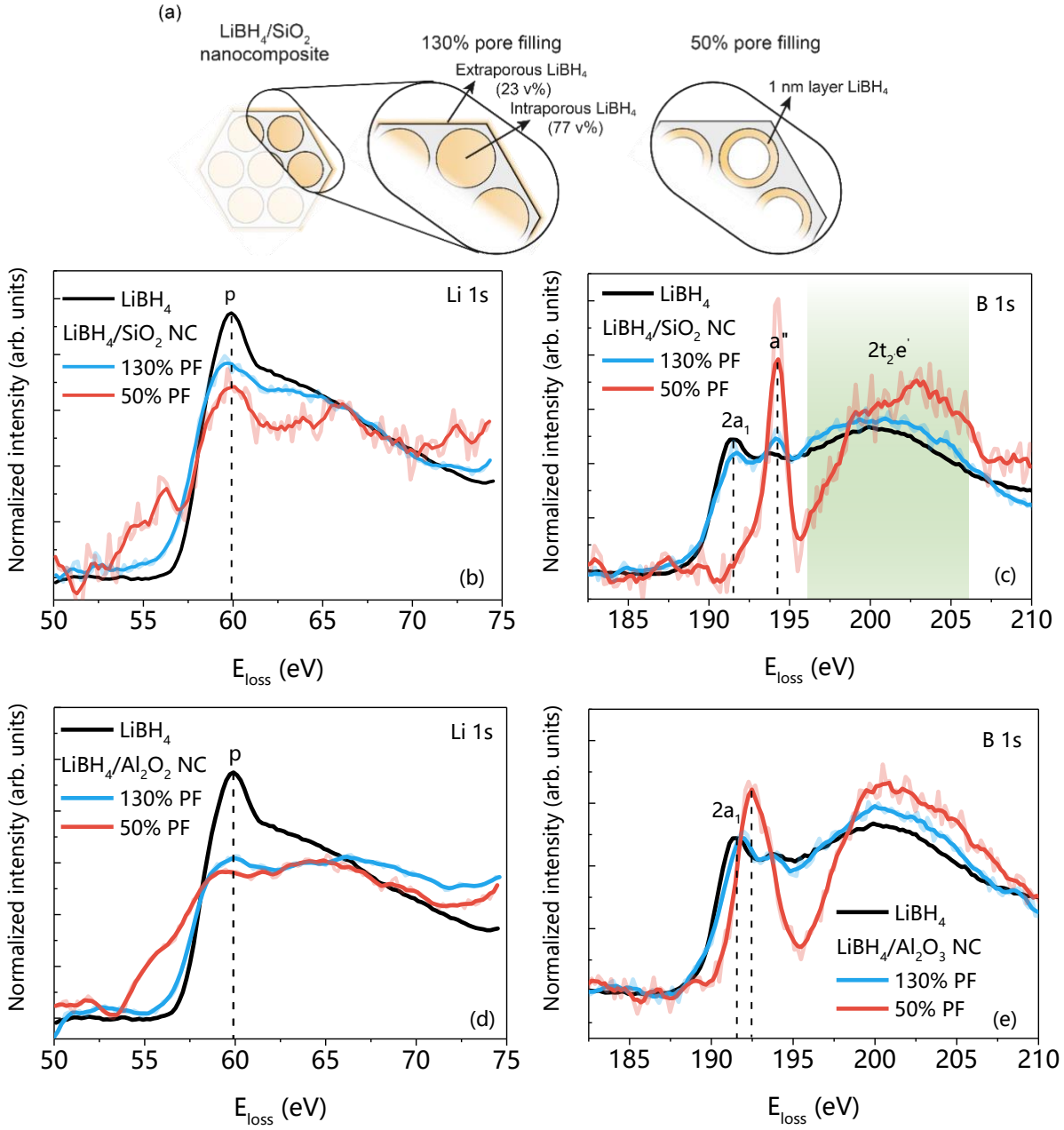

Figure 3. (a) Schematic representations of $LiBH_4/SiO_2$ nanocomposites with 130% and 50% of the oxide pores filled with $LiBH_4$. (b, d) Li K-edge and (c, e) B K-edge XRS spectra of pristine $LiBH_4$ powder (95% purity) and $LiBH_4$/oxide nanocomposites based on SiO_2 and Al_2O_3 with 130% and 50% PF. The spectra of nanocomposites are smoothened using adjacent averaging over 5 points.

Similarly, in the B K-edge spectra (**Figure 3c**), clear changes are observed when comparing pristine $LiBH_4$ to the $LiBH_4/SiO_2$ nanocomposites. In the spectrum of the nanocomposite with 130 % pore filling, the peak at 191.5 eV associated with the tetrahedral $2a_1$ transition is less intense compared to the spectrum of pristine $LiBH_4$, while the feature attributed to trigonal boron is more intense and appears at a slightly more positive energy (194.2 eV). In the B K-edge spectra of the nanocomposites with 50% (**Figure 3c**) and 15% PF (**Figure S1**), the characteristic $[BH_4]$ a_1 peak observed at 191.5 eV is not present anymore. Instead, the feature at 194.2 eV, which corresponds to trigonal B, has transformed into a prominent and well-defined peak. The change in the ratio between the tetrahedral and the trigonal boron peaks shows that the nanocomposites contain significantly more trigonal boron than pristine $LiBH_4$, especially in the nanocomposites with a lower pore-filling fraction. It strongly suggests that upon nanocomposite formation with the mesoporous silica, an interface reaction occurs between $LiBH_4$ and the oxide, resulting in the formation of trigonal boron compounds from BH_4^-.

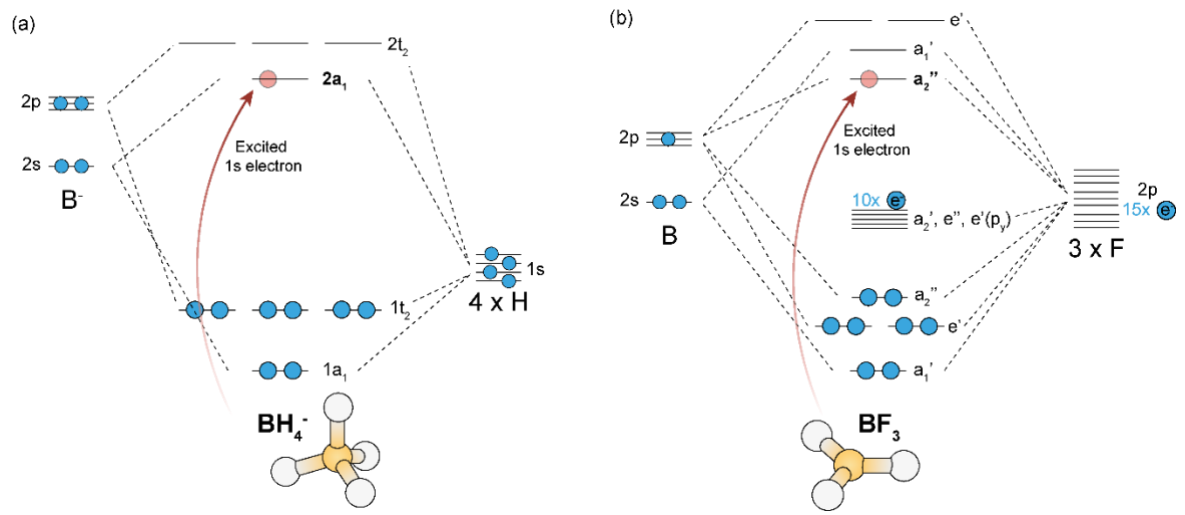

Figure 4. Schematic representation of the molecular orbital diagrams of (a) BH_4^- and (b) BF_3 based on symmetry adapted linear combinations (SALCs). The corresponding molecular geometries, i.e., tetrahedral for BH_4^- and trigonal planar for BF_3, are provided as well.

While these analyses provide general information about the chemical environment of lithium and boron in the nanocomposites, the precise interface composition remains unclear. Therefore, to obtain more detailed information, the spectra were fitted using a linear combination of available relevant reference compounds **(Figure S2)**. The experimental data of the $LiBH_4/SiO_2$ nanocomposites was fitted with the B K-edge spectra of pristine $LiBH_4$, $Li_2B_{12}H_{12}$, $LiBO_2$, and H_3BO_3 (**Figure S3**) to distinguish between the tetrahedral and trigonal boron species present. It should be noted that the trigonal boron species in the nanocomposites could also be based on hydrogen (e.g., BH_3), especially as both $LiBO_2$ and H_3BO_3 are not ionically conductive. However, there are no suitable references for this configuration. The resulting linear combination fits are plotted in **Figure S3,** and the corresponding fitting parameters are given in **Table S1**. Although not perfect, a comparison of the linear combination fits to the measured data indicates that the model explains the data to a reasonable/acceptable extent (adjusted $R^2 > 0.83$), The origin of the limitation will be explained later.

The linear combination fit of the $LiBH_4/SiO_2$ nanocomposite with 130% pore filling confirms that the nanocomposite consists largely of $LiBH_4$ **(Figure S3a)**. A small amount of $Li_2B_{12}H_{12}$, a well-known decomposition product of $LiBH_4$, is observed as well. Furthermore, the trigonal feature at 194.2 eV can be fitted with a combination of the B-O species, essentially resembling $LiBO_2$ and partially resembling H_3BO_3. Note that in the fit, the peak around 191.5 eV has a higher intensity compared to the experimental data. Hence, either the amount of $LiBH_4$ or $Li_2B_{12}H_{12}$ present in the nanocomposite is overestimated, or the anions contain more negative charge (possibly due to the formation of Li^+ vacancies). In the nanocomposites with lower pore filling fractions, i.e., 50%, the contributions of $LiBH_4$ and $Li_2B_{12}H_{12}$ are not considered since the characteristic peak around 191.5 eV is not present in these samples **(Figure S3b and S3c)**. Instead, the experimental data is fitted solely with the trigonal reference compounds. Based on the resulting linear combination fits of both nanocomposites, it seems that a mixture of trigonal boron phases is present at the $LiBH_4$ – SiO_2 interface.

Interestingly, the ratio between $LiBO_2$ and H_3BO_3 characters in the $LiBH_4/SiO_2$ nanocomposites changes upon going from 50% PF to 15% PF (Table S1). The fitting parameter of the $LiBO_2$ contribution becomes smaller, while the fitting parameter of the H_3BO_3 contribution becomes larger. It appears that closer to the SiO_2 surface, the interface layer between metal hydride and oxide contains compounds where the energy associated with the trigonal a'' transition shifts to higher values. This phenomenon is observed in compounds like H_3BO_3 when compared to $LiBO_2$. This suggests that the structure within the interface layer differs depending on the proximity of the oxide or metal hydride. Additionally, it might be influenced by interactions with the different silanol groups on the SiO_2 surface. These groups include surface siloxanes, isolated, geminal, and vicinal silanols, each of which slightly varies in their chemical bonds.[66]

It is important to note that the interface layer is a highly defective and distorted phase. These defects and distortions can greatly affect the local chemical environment of the boron species. The B K-edge spectra **(Figure 3c)** illustrate that the $LiBH_4$ – SiO_2 interface layer contains trigonal boron (such as $LiBO_2$ or BH_3). However, the precise chemical environment will be different from the purely crystalline phases that have been measured as reference compounds. The same is true for the chemical environment of Li^+. While the Li K-edge spectra exhibit features that can be attributed to the presence of Li_2O, it is more likely that these features are related to the formation of Li-O bonds. In summary, our observations are in accordance with the formation of a Si-H-BH_3 like structure and Li-O (or more precisely Si-O-Li) bond via the reduction of a siloxane bond as proposed by Lambregts *et al*., though the formation of the Si-O-Li-BH_3 structure discussed by Dou, and Wang, *et al*. cannot be excluded, as both cases result in trigonal boron.[29, 33, 34] We also observed the formation of a Li^+-compound that has a weak interaction with the surrounding anions. This is in accordance with the reduced activation energies for ionic transport in $LiBH_4/SiO_2$ nanocomposites (0.4 – 0.5 eV) compared to pristine $LiBH_4$(0.7 - 0.9 eV), [16, 53, 67, 68] and could explain the enhanced ionic conductivity upon nanocomposite formation. For a more definite understanding of the precise chemical environment at the interface, the utilization of model systems in combination with theoretical simulations is required.

$NaBH_4$ and $NaNH_2$/Oxide Nanocomposites

Following a methodology similar to the investigation conducted on the Li-ion conductor $LiBH_4$, the effect of nanocomposite formation on the chemical structure of the Na-ion conductors $NaBH_4$ and $NaNH_2$ was examined. This was achieved by studying $NaBH_4/SiO_2$ and $NaNH_2/SiO_2$ nanocomposites with different (PF) fractions. In **Figures 5a and c,** the B and Na K-edge XRS spectra of pristine $NaBH_4$ and $NaBH_4/SiO_2$ nanocomposites with 30 and 100 %PF are depicted, while the spectra of some relevant reference compounds are shown in **Figure S4a-c**.

In the B K-edge spectra of the $NaBH_4/SiO_2$ nanocomposites (**Figure 5a**), evident distinctions from the pristine $NaBH_4$ spectrum are observed. The peak at 191.7 eV, associated with the $2a_1$ transition of tetrahedral B (in BH_4^-), becomes less intense upon nanocomposite formation. At the same time, the spectra of the nanocomposites contain a feature at 194.1 eV, which is not observed in pristine $NaBH_4$. Based on **Figure 4**, the peak around 194 eV is attributed to the transition of B 1s electrons to unoccupied a'' orbitals of trigonal boron, such as BO_2^- and H_3BO_3. In the $NaBH_4/SiO_2$ nanocomposite with 30% pore filling, the peak related to $NaBH_4$ is smaller than the peak corresponding to trigonal boron. Thus, at the interface between $NaBH_4$ and SiO_2, a layer consisting of trigonal boron, Na-O, and weakly coordinated Na^+ seems to form, similar to the interface layer between $LiBH_4$ and SiO_2.

The Na K-edge spectra of the $NaBH_4/SiO_2$ nanocomposites (**Figure 5c**) are compared to that of the pristine $NaBH_4$. In the spectrum of pristine $NaBH_4$, two peaks are observed at 1076.2 eV and 1078.9 eV. These peaks are attributed to the transition of a 1s electron to an unoccupied 3p state of $NaBH_4$.[69, 70] The Na K-edge spectrum of $NaBH_4/SiO_2$ with 30% PF contains an additional pre-edge peak at 1073.9 eV and a broad feature around 1082 eV. As similar changes were also observed in the Li K-edge spectra of $LiBH_4/SiO_2$, (**Figure 3b**), this points to the formation of Na^+ bonded to, or in closer proximity to O, as well as Na^+ that weakly interacts with the anion (highly distorted BH_4 or BH_3).

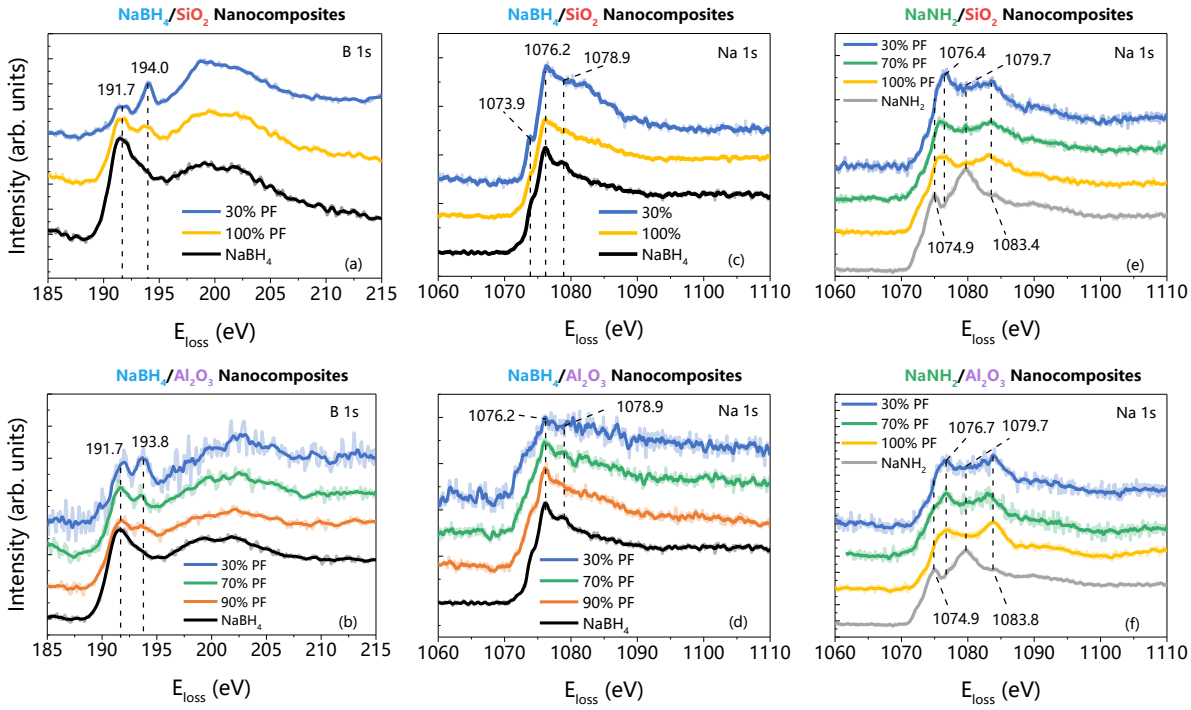

Figure 5. (a, b) B K-edges (c, d) Na K-edges of $NaBH_4/SiO_2$ and $NaBH_4/Al_2O_3$ nanocomposites, respectively. (e, f) Na K-edges of $NaNH_2/SiO_2$ and $NaNH_2/Al_2O_3$ nanocomposites, respectively. The spectra of the pristine $NaBH_4$ and $NaNH_2$ are added for reference. The spectra are smoothened using adjacent averaging over 5 points.

Analogous to the $NaBH_4/SiO_2$, the interfacial interaction in $NaNH_2/SiO_2$ nanocomposites was investigated. In **Figure 5f,** it is quite clear that when confined in mesoporous SiO_2, $NaNH_2$ exhibits more profound changes in the Na K-edge compared to $NaBH_4$ as the two characteristics peaks are both shifted to much higher energy loss values than in $NaBH_4/SiO_2$ (**Figure 5c**). The shift to the higher energy loss is due to the formation of a Na-N-O_x-H_y-like compound (as in $NaNO_2$ or $NaNO_3$) at the $NaNH_2/SiO_2$ interface (See **Figure S4c**), in which N has a higher binding energy than in $NaNH_2$. This is a clear evidence that $NaNH_2$ reacts with SiO_2 surface groups to form an interface compound that is distinct and more conductive than the original $NaNH_2$. The presence of N-O bond is also a major indication that the interface compounds in $LiBH_4$ and $NaBH_4$-based nanocomposites indeed contain "B-O like" bonds.

Effects of the Nanoscaffolds: SiO_2 versus Al_2O_3

The nature of the oxide scaffolds has been reported to have a profound impact on the conductivity of enhancements in composite electrolytes.[13, 16, 19] Therefore, it is interesting to study the effect of the chemical nature of the oxide scaffolds on the interface chemistry/composition. In line with this objective, we also measured the XRS spectra of nanocomposites prepared with mesoporous γ-Al_2O_3, another widely employed oxide. **Figure 3b-e and 5a-f** compare the K-edge spectra of the $LiBH_4$-, $NaBH_4$ and $NaNH_2$-based nanocomposites prepared using SiO_2 and Al_2O_3. A comparison of **Figures 3b** and **3d** shows major similarities, but also minor differences, between the Li K-edge spectra of $LiBH_4/SiO_2$ and $LiBH_4/Al_2O_3$. At low $LiBH_4$ concentration (50 % PF), a minor peak is observed around 62 eV in $LiBH_4/Al_2O_3$ which is not obvious in $LiBH_4/SiO_2$. This reveals that the chemical environment (nature/composition) of Li is mostly, but not completely, similar to the SiO_2 and Al_2O_3-based nanocomposites. This is remarkably in agreement with previous reports of similar ionic conductivities and activation energies of 0.43 eV and 0.44 eV, respectively for $LiBH_4/SiO_2$ and $LiBH_4/Al_2O_3$ prepared in the same manner.[16, 28] However, note that the conductivity might vary if the specific surface area, pore volume and/or pore size of the oxide is changed.

For the B K-edge spectra, although similarities exist, there are more notable dissimilarities between the two samples. Analogous to $LiBH_4/SiO_2$, $LiBH_4/Al_2O_3$ contains the a'' peak around 194.1 eV indicative of interfacial trigonal boron compounds, and the peak at 191.5 eV which corresponds to BH_4^- becomes smaller with lower $LiBH_4$ concentration (pore filling). In contrast, in $LiBH_4/Al_2O_3$, the a'' peak is broader and at a slightly lower energy loss value (~193.7 eV) than for SiO_2. Intriguingly, the peak shifts to energy loss values similar to $LiBH_4/SiO_2$ (194.1 eV) when the concentration of $LiBH_4$ is reduced to 15 % PF (see **Figure S1**). This is a clear indication of a significant difference in the local environments of the interfacial boron compounds in SiO_2 and Al_2O_3. The origin of these differences will be discussed later, although it appears the differences have negligible impact on the ionic conductivity.

For the B K-edges (**Figure 5a and b),** the position of the peak attributed to the interface trigonal boron is shifted from approximately 194.1 eV in $NaBH_4/SiO_2$ to approximately 193.7 eV in $NaBH_4/SiO_2$. This implies a slightly different chemical environment for B in SiO_2 and Al_2O_3-based samples, as observed in the $LiBH_4$/oxide nanocomposites. From **Figure 5c and d**, it can be seen that although the Na K-edges of $NaBH_4$ looks similar in the Al_2O_3 and SiO_2-based nanocomposites, the pre-peak feature at 1073.9 eV in $NaBH_4/SiO_2$ is absent in $NaBH_4/Al_2O_3$. Extending the comparison to $NaNH_2/SiO_2$ versus $NaNH_2/Al_2O_3$ (**Figure 5e and f**), it is clear that the two main peaks of the Na K-edge spectra are located at a slightly higher energy loss values in Al_2O_3 than in SiO_2. Specifically, from 1076.4 eV and 1083.4 eV in $NaNH_2/SiO_2$ to 1076.7 and 1083.8 eV in $NaNH_2/Al_2O_3$. This suggests that $NaNH_2$ forms a slightly more stable (higher binding energy) interface compound with Al_2O_3 than with SiO_2,which could explain why the $NaNH_2/SiO_2$ is far more conductive than the $NaNH_2/Al_2O_3$

These differences in the nature of the interface compounds for SiO_2 and Al_2O_3 can be attributed to the differences in the chemical nature or surface chemistry and acidity of the two oxides, which dictates the nature of the surface reaction. For example, the surface of silica generally contains about 4 to 5.5 hydroxyl groups per nm^2, which are weak Brønsted acidic sites, while the surface of γ-Al_2O_3 contains between 10 and 15 hydroxyl groups per nm^2, both Brønsted bases and Brønsted acids. In addition, the uncoordinated (also called pentacoordinated) Al-sites give rise to Lewis acid sites in Al_2O_3, which does not exist in SiO_2.[71-75]Thus, it is expected that the cation (Li^+ or Na^+) and the complex anion (BH_4^- or NH_2^-) in the molten metal hydride will interact differently with the γ-Al_2O_3 and SiO_2 surfaces. For example, if BH_4^- or NH_2^- interacts with an uncoordinated Al-site instead of an acidic hydroxyl group, the tetrahedral boron configuration might remain intact rather than forming a trigonal boron compound. As a result, the energy of the 1s to $2a_1$ transition would shift to slightly different values compared to the latter case. This means that at least two different interfacial B species would be expected, arising from the BH_4^- interacting with an uncoordinated Al site, and those bonded to the hydroxyl groups.

Likewise, the presence of a more stable interfacial compound in $NaNH_2/Al_2O_3$ than in $NaNH_2/SiO_2$ can be related to the strong Lewis acid/basic sites of the Al_2O_3, which will expectedly lead to a stronger interaction with the complex hydrides. To assign these subtle differences in the chemical environment of the elements to specific compounds in the metal hydride-oxide interfacial layer, the experimental data need to be supported by ab initio simulations. While this is a topic for a future project, we have successfully showcased that the interface layer in metal hydride/alumina nanocomposites exhibits a markedly different composition compared to metal hydride/silica nanocomposites. It is remarkable that both scenarios lead to the creation of highly conductive nanocomposites.

Correlation of Interface Composition to Ionic Conductivity

Based on the XRS results discussed in the previous sections, it is clear that the interphases in nanocomposite electrolytes depend strongly on the type of oxide scaffold used. This agrees with the conductivity results (**Figure S5**), and previous studies that highlight the strong impacts of the metal oxide type on the conductivity of the nanocomposites. Notably, the impact on conductivity differs among the three hydride-based ion conductors studied here. For emphasis, higher conductivity is obtained for $NaNH_2/SiO_2$ than $NaNH_2/Al_2O_3$ while the reverse is the case for $NaBH_4/SiO_2$ and $NaBH_4/Al_2O_3$. As explained in detail in our recent work, this behavior is a result of the complex interplay between the nature or reactivity of the oxide surface groups and the stability or reactivity of the ionically conductive metal hydrides. These properties dictate the accurate hydride-oxide reaction/interaction, hence the nature, stability, and conductivity of the interface compounds. For example, the lower conductivity of $NaNH_2/Al_2O_3$ compared to $NaNH_2/SiO_2$ can be attributed to the formation of a more chemically stable (less defected) interface compound with Al_2O_3 than with SiO_2, as revealed by the XRS results.

Due to differences in the physical properties of the oxides (surface area, pore size, pore volume and morphology) which are known to also influence ionic conductivity, it is not straightforward to

compare these oxides on the same scale. To overcome this limitation and thereby establish a link between the interface layer and conductivity, we explored the concept of surface functionalization by grafting. For this, we prepared aluminium- and zirconium-grafted SiO_2 and studied the conductivity and interface composition of $LiBH_4$/oxide nanocomposites based on these grafted SiO_2 nanoscaffolds. The surface chemistry of the Al- and Zr-grafted SiO_2 scaffolds differs from pristine SiO_2[19, 76-78], while their physical properties (e.g., surface area, pore volume, morphology) are the same. In this way, the strength of the interface interaction can be tuned, making it possible to uniquely determine how the ionic conductivity is influenced by the $LiBH_4$-SiO_2 interface composition.

In **Figure 6a**, the B K-edge XRS spectra of $LiBH_4$/M-SiO_2 nanocomposites (M = Al and Zr) with 130% pore filling are reported. Surprisingly, the peak at 191.5 eV decreases in intensity when going from SiO_2 to Al-SiO_2 to Zr-SiO_2, while the peak at 194.0 eV increases. This suggests a reduction in the number of tetrahedral boron species, namely BH_4-, alongside an increase in the prevalence of trigonal boron compounds. The interface interaction between $LiBH_4$ and Zr-SiO_2 is stronger (Zr is a stronger Lewis acid than Al and SiO_2), and as a result, more $LiBH_4$ is converted to trigonal B interface species. In other words, the interphase extends further from the interface, or more interface compound is present. Notably, the conductivity data **(Figure 6b)** manifests a strong correlation between the interaction strength or composition of the $LiBH_4$-oxide interface and the ion conductivity. At 30 °C, $LiBH_4$/SiO_2 exhibits a conductivity of $0.2 \cdot 10^{-5}$ S cm^{-1}, whereas the $LiBH_4$/Al-SiO_2 and $LiBH_4$/Zr-SiO_2 nanocomposites exhibit higher conductivities of $1.4 \cdot 10^{-5}$ S cm^{-1} and $5.1 \cdot 10^{-5}$ S cm^{-1}, respectively. These results clearly underscore the fact that $LiBH_4$/oxide nanocomposites with more trigonal boron species exhibit higher conductivity. Therefore, our study reveals that the formation of more trigonal boron also corresponds to the formation of a more highly defected interphase and/or weakly coordinated Li-ions. As a result, this facilitates fast Li-ion transport in nanocomposites based on $LiBH_4$ and $NaBH_4$.

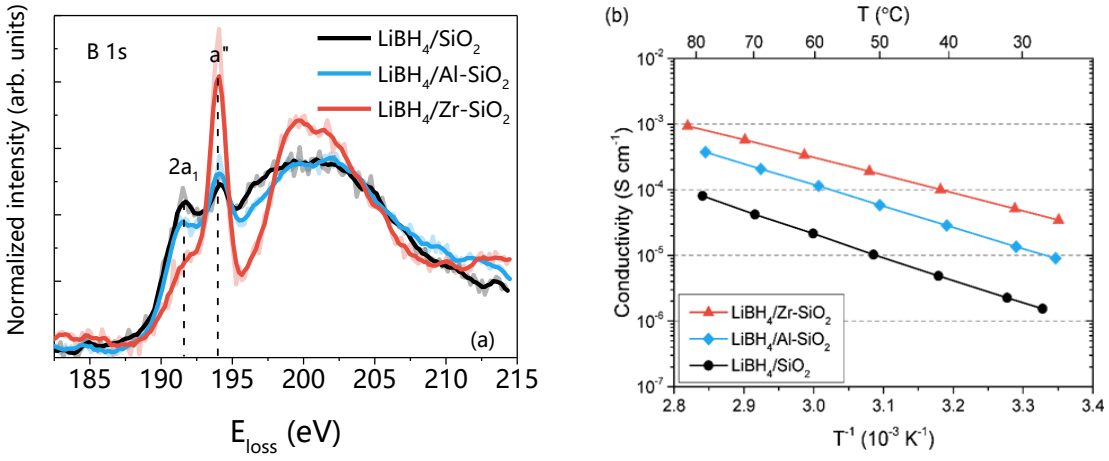

Figure 6. (a) B K-edge XRS spectra of $LiBH_4/SiO_2$, $LiBH_4$/Al-SiO_2 and $LiBH_4$/Zr-SiO_2 nanocomposites with pore filling fraction of 130%. The spectra are smoothened using adjacent averaging over 5 points. (b) Arrhenius plots of conductivity versus reciprocal temperature of $LiBH_4/SiO_2$, $LiBH_4$/Al-SiO_2 and $LiBH_4$/Zr-SiO_2.

Conclusions

XRS has been utilized to decipher the nature of ion conductor/insulator interfaces leading to high conductivities in composite solid electrolytes, specifically, nanocomposites containing complex hydrides ($LiBH_4$, $NaBH_4$, and $NaNH_2$) and metal oxides. Investigation of the local environment of Li, Na, and B shows that these ionic conductors react with the oxide's (SiO_2 and Al_2O_3) surface groups upon nanocomposite formation. This results in the formation of an interphase at the metal hydride/oxide interface. For the boron-based hydrides ($LiBH_4$ and $NaBH_4$), the original tetragonal (BH_4) structure transforms into mostly trigonal boron such as -BH_3 with a "B-O" like character. Likewise, for $NaNH_2$, a clear indication of the N-O bond is observed at the interface, a major validation of the reaction of the hydrides with the surface OH groups. Moreover, in this interphase, part of the Li and Na are connected to oxygen, suggesting an M-O bond at the interface. While unveiling the intricate structure of the metal hydride-oxide interface poses challenges, the XRS results show that the formed interphase is strongly influenced by the physico-chemical properties of the oxide employed. Remarkably, nanocomposites with higher concentrations of the interface compound also exhibit higher ionic conductivities. Therefore, our work reveals that surface reactions play a dominant role in interfacial ion dynamics and

establishes for the first time that a direct correlation exists between the nature of the interphase and ion mobility in nanocomposite solid electrolytes. This fundamental insight is of utmost importance for the rational design of novel superionic conductors via interface engineering. Furthermore, these findings underscore the potential of XRS as a promising technique for studying battery materials and interfaces with often low atomic weight. These aspects are not easily explored by conventional techniques.

Acknowledgment

The authors express their appreciation for the financial support provided by the Netherlands Organization for Scientific Research(NWO) materials for sustainability (Mat4Sus) grant (739.017.009), as well as the Battery NL Funding. The European Synchrotron Radiation Facility (ESRF: ID20) Grenoble France and beamline P01 at PETRA III (DESY), Hamburg, Germany are thanked for the beam time and support for this research. Marcel Van Asselen and Sander Deelen are acknowledged for their help in the design of the in situ XRS cell.

References

(1) Armand, M.; Tarascon, J. M. Building better batteries. *Nature* **2008**, *451* (7179), 652-657. DOI: 10.1038/451652a.

(2) Sun, C.; Liu, J.; Gong, Y.; Wilkinson, D. P.; Zhang, J. Recent advances in all-solid-state rechargeable lithium batteries. *Nano Energy* **2017**, *33*, 363-386. DOI: https://doi.org/10.1016/j.nanoen.2017.01.028.

(3) Wu, F.; Maier, J.; Yu, Y. Guidelines and trends for next-generation rechargeable lithium and lithium-ion batteries. *Chemical Society Reviews* **2020**, *49* (5), 1569-1614, 10.1039/C7CS00863E. DOI: 10.1039/C7CS00863E.

(4) Zhang, Z.; Shao, Y.; Lotsch, B.; Hu, Y.-S.; Li, H.; Janek, J.; Nazar, L. F.; Nan, C.-W.; Maier, J.; Armand, M.; et al. New horizons for inorganic solid state ion conductors. *Energy & Environmental Science* **2018**, *11* (8), 1945-1976, 10.1039/C8EE01053F. DOI: 10.1039/C8EE01053F.

(5) Janek, J.; Zeier, W. G. A solid future for battery development. *Nature energy* **2016**, *1* (9), 1-4.

(6) Famprikis, T.; Canepa, P.; Dawson, J. A.; Islam, M. S.; Masquelier, C. Fundamentals of inorganic solid-state electrolytes for batteries. *Nature materials* **2019**, *18* (12), 1278-1291.

(7) Zhao, Q.; Stalin, S.; Zhao, C.-Z.; Archer, L. A. Designing solid-state electrolytes for safe, energy-dense batteries. *Nature Reviews Materials* **2020**, *5* (3), 229-252.

(8) Ameloot, R.; Aubrey, M.; Wiers, B. M.; Gómora-Figueroa, A. P.; Patel, S. N.; Balsara, N. P.; Long, J. R. Ionic Conductivity in the Metal–Organic Framework UiO-66 by Dehydration and Insertion of Lithium tert-Butoxide. *Chemistry – A European Journal* **2013**, *19* (18), 5533-5536. DOI: https://doi.org/10.1002/chem.201300326.

(9) Zettl, R.; Lunghammer, S.; Gadermaier, B.; Boulaoued, A.; Johansson, P.; Wilkening, H. M. R.; Hanzu, I. High Li+ and Na+ Conductivity in New Hybrid Solid Electrolytes based on the Porous MIL-121 Metal Organic Framework. *Advanced Energy Materials* **2021**, *11* (16), 2003542. DOI: https://doi.org/10.1002/aenm.202003542.

(10) Le, T.-T.; Abbas, M.; Dreistadt, D. M.; Klassen, T.; Pistidda, C. Ionic conductivity in complex hydrides for energy storage applications: A comprehensive review. *Chemical Engineering Journal* **2023**, *473*, 145315. DOI: https://doi.org/10.1016/j.cej.2023.145315.

(11) Liang, C. C. Conduction Characteristics of the Lithium Iodide-Aluminum Oxide Solid Electrolytes. *Journal of The Electrochemical Society* **1973**, *120* (10), 1289. DOI: 10.1149/1.2403248.

(12) Agrawal, R. C.; Gupta, R. K. Superionic solid: composite electrolyte phase – an overview. *Journal of Materials Science* **1999**, *34* (6), 1131-1162. DOI: 10.1023/A:1004598902146.

(13) Zou, Z.; Li, Y.; Lu, Z.; Wang, D.; Cui, Y.; Guo, B.; Li, Y.; Liang, X.; Feng, J.; Li, H. Mobile ions in composite solids. *Chemical reviews* **2020**, *120* (9), 4169-4221.

(14) Uvarov, N. F.; Hairetdinov, E. F.; Skobelev, I. V. Composite solid electrolytes MeNO3-Al2O3 (Me = Li, Na, K). *Solid State Ionics* **1996**, *86-88*, 577-580. DOI: https://doi.org/10.1016/0167-2738(96)00208-1.

(15) de Kort, L. M.; Gulino, V.; de Jongh, P. E.; Ngene, P. Ionic conductivity in complex metal hydride-based nanocomposite materials: The impact of nanostructuring and nanocomposite formation. *Journal of Alloys and Compounds* **2022**, *901*, 163474. DOI: https://doi.org/10.1016/j.jallcom.2021.163474.

(16) Gulino, V.; Barberis, L.; Ngene, P.; Baricco, M.; De Jongh, P. E. Enhancing Li-ion conductivity in LiBH4-based solid electrolytes by adding various nanosized oxides. *ACS Applied Energy Materials* **2020**, *3* (5), 4941-4948.

(17) Zhou, C.; Sun, H.; Wang, Q.; Grinderslev, J. B.; Liu, D.; Yan, Y.; Jensen, T. R. Highly electrochemically stable Li2B12H12-Al2O3 nanocomposite electrolyte enabling A 3.8 V room-temperature all-solid-state Li-ion battery. *Journal of Alloys and Compounds* **2023**, *938*, 168689.

(18) de Kort, L. M.; Brandt Corstius, O. E.; Gulino, V.; Gurinov, A.; Baldus, M.; Ngene, P. Designing Highly Conductive Sodium-Based Metal Hydride Nanocomposites: Interplay between Hydride and Oxide Properties. *Advanced Functional Materials* **2023**, *33* (13), 2209122. DOI: https://doi.org/10.1002/adfm.202209122.

(19) De Kort, L. M.; Harmel, J.; De Jongh, P. E.; Ngene, P. The effect of nanoscaffold porosity and surface chemistry on the Li-ion conductivity of LiBH 4–LiNH 2/metal oxide nanocomposites. *Journal of Materials Chemistry A* **2020**, *8* (39), 20687-20697.

(20) Cuevas, F.; Amdisen, M. B.; Baricco, M.; Buckley, C. E.; Cho, Y. W.; de Jongh, P.; de Kort, L. M.; Grinderslev, J. B.; Gulino, V.; Hauback, B. C.; et al. Metallic and complex hydride-based electrochemical storage of energy. *Progress in Energy* **2022**, *4* (3), 032001. DOI: 10.1088/2516-1083/ac665b.

(21) de Kort, L. M.; Harmel, J.; de Jongh, P. E.; Ngene, P. The effect of nanoscaffold porosity and surface chemistry on the Li-ion conductivity of LiBH4–LiNH2/metal oxide nanocomposites. *Journal of Materials Chemistry A* **2020**, *8* (39), 20687-20697, 10.1039/D0TA07600G. DOI: 10.1039/D0TA07600G.

(22) de Kort, L.; Ngene, P.; Baricco, M.; de Jongh, P.; Gulino, V. Improving the Cycle Life of Solid-State Batteries by Addition of Oxide Nanoparticles to a Complex Hydride Solid Electrolyte. *The Journal of Physical Chemistry C* **2023**, *127* (8), 3988-3995. DOI: 10.1021/acs.jpcc.2c08902.

(23) Das, S.; Ngene, P.; Norby, P.; Vegge, T.; De Jongh, P. E.; Blanchard, D. All-solid-state lithium-sulfur battery based on a nanoconfined LiBH4 electrolyte. *Journal of The Electrochemical Society* **2016**, *163* (9), A2029.

(24) Gulino, V.; Brighi, M.; Murgia, F.; Ngene, P.; de Jongh, P.; Černý, R.; Baricco, M. Room-Temperature Solid-State Lithium-Ion Battery Using a LiBH4–MgO Composite Electrolyte. *ACS Applied Energy Materials* **2021**, *4* (2), 1228-1236. DOI: 10.1021/acsaem.0c02525.

(25) Maier, J. Space charge regions in solid two-phase systems and their conduction contribution—I. Conductance enhancement in the system ionic conductor-'inert' phase and application on AgC1:Al2O3 and AgC1:SiO2. *Journal of Physics and Chemistry of Solids* **1985**, *46* (3), 309-320. DOI: https://doi.org/10.1016/0022-3697(85)90172-6.

(26) Maier, J. Ionic conduction in space charge regions. *Progress in Solid State Chemistry* **1995**, *23* (3), 171-263. DOI: https://doi.org/10.1016/0079-6786(95)00004-E.

(27) Zheng, Y. B.; Huang, T. J. Surface plasmons of metal nanostructure arrays: From nanoengineering to active plasmonics. *Journal of the Association for Laboratory Automation* **2008**, *13* (4), 215-226.

(28) Choi, Y. S.; Lee, Y.-S.; Choi, D.-J.; Chae, K. H.; Oh, K. H.; Cho, Y. W. Enhanced Li Ion Conductivity in LiBH4–Al2O3 Mixture via Interface Engineering. *The Journal of Physical Chemistry C* **2017**, *121* (47), 26209-26215.

(29) Dou, Y.; Hansen, H. A.; Xu, S.-M.; Blanchard, D. Layered double hydroxides as advanced tracks to promote ionic conductivity in metal borohydride. *Materials Chemistry Frontiers* **2021**, *5* (13), 4989-4996.

(30) Luo, X.; Rawal, A.; Aguey-Zinsou, K.-F. Investigating the factors affecting the ionic conduction in nanoconfined NaBH4. *Inorganics* **2021**, *9* (1), 2.

(31) Zhao, W.; Zhang, R.; Li, H.; Zhang, Y.; Wang, Y.; Wu, C.; Yan, Y.; Chen, Y. Li-Ion Conductivity Enhancement of LiBH4· x NH3 with In Situ Formed Li2O Nanoparticles. *ACS Applied Materials & Interfaces* **2021**, *13* (27), 31635-31641.

(32) Liu, Z.; Xiang, M.; Zhang, Y.; Shao, H.; Zhu, Y.; Guo, X.; Li, L.; Wang, H.; Liu, W. Lithium migration pathways at the composite interface of LiBH 4 and two-dimensional MoS 2 enabling superior ionic conductivity at room temperature. *Physical Chemistry Chemical Physics* **2020**, *22* (7), 4096-4105.

(33) Hwang, S.-J.; Lee, H.-S.; To, M.; Lee, Y.-S.; Cho, Y. W.; Choi, H.; Kim, C. Probing molecular dynamics of metal borohydrides on the surface of mesoporous scaffolds by multinuclear high resolution solid state NMR. *Journal of Alloys and Compounds* **2015**, *645*, S316-S319.

(34) Lambregts, S. F.; Van Eck, E. R.; Ngene, P.; Kentgens, A. P. The Nature of Interface Interactions Leading to High Ionic Conductivity in LiBH4/SiO2 Nanocomposites. *ACS Applied Energy Materials* **2022**, *5* (7), 8057-8066.

(35) Miedema, P. S. Raman Spectroscopy with X-Rays. In *Raman Spectroscopy and Applications*, IntechOpen Rijeka, 2017.

(36) Bergmann, U.; Glatzel, P.; Cramer, S. P. Bulk-sensitive XAS characterization of light elements: from X-ray Raman scattering to X-ray Raman spectroscopy. *Microchemical Journal* **2002**, *71* (2), 221-230. DOI: https://doi.org/10.1016/S0026-265X(02)00014-0.

(37) Schülke, W. *Electron dynamics by inelastic X-ray scattering*; OUP Oxford, 2007.

(38) Huotari, S.; Pylkkänen, T.; Verbeni, R.; Monaco, G.; Hämäläinen, K. Direct tomography with chemical-bond contrast. *Nature materials* **2011**, *10* (7), 489.

(39) Miedema, P. S.; Ngene, P.; Van Der Eerden, A. M.; Sokaras, D.; Weng, T.-C.; Nordlund, D.; Au, Y. S.; De Groot, F. M. In situ X-ray Raman spectroscopy study of the hydrogen sorption properties of lithium borohydride nanocomposites. *Physical Chemistry Chemical Physics* **2014**, *16* (41), 22651-22658.

(40) Miedema, P. S.; Ngene, P.; van der Eerden, A. M.; Weng, T.-C.; Nordlund, D.; Sokaras, D.; Alonso-Mori, R.; Juhin, A.; de Jongh, P. E.; de Groot, F. M. In situ X-ray Raman spectroscopy of LiBH 4. *Physical Chemistry Chemical Physics* **2012**, *14* (16), 5581-5587.

(41) Fehse, M.; Sahle, C. J.; Hogan, M. P.; Cavallari, C.; Kelder, E. M.; Alfredsson, M.; Longo, A. Bulk-sensitive soft X-ray edge probing for elucidation of charge compensation in battery electrodes. *The Journal of Physical Chemistry C* **2019**, *123* (40), 24396-24403.

(42) Rajh, A.; Arčon, I.; Bučar, K.; Žitnik, M.; Petric, M.; Vizintin, A.; Bitenc, J.; Košir, U.; Dominko, R.; Gretarsson, H. Characterization of Electrochemical Processes in Metal–Organic Batteries by X-ray Raman Spectroscopy. *The Journal of Physical Chemistry C* **2022**, *126* (12), 5435-5442.

(43) Sahle, C. J.; Kujawski, S.; Remhof, A.; Yan, Y.; Stadie, N. P.; Al-Zein, A.; Tolan, M.; Huotari, S.; Krisch, M.; Sternemann, C. In situ characterization of the decomposition behavior of Mg (BH 4) 2 by X-ray Raman scattering spectroscopy. *Physical Chemistry Chemical Physics* **2016**, *18* (7), 5397-5403.

(44) Nonaka, T.; Kawaura, H.; Makimura, Y.; Nishimura, Y. F.; Dohmae, K. In situ X-ray Raman scattering spectroscopy of a graphite electrode for lithium-ion batteries. *Journal of Power Sources* **2019**, *419*, 203-207.

(45) Tack, P.; De Pauw, E.; Tkalcec, B.; Longo, A.; Sahle, C. J.; Brenker, F.; Vincze, L. Identification of the Calcium, Aluminum, and Magnesium Distribution within Millimeter-Sized Extraterrestrial Materials Using Nonresonant X-ray Raman Spectroscopy in Preparation for the Hayabusa2 Sample Return Mission. *Analytical Chemistry* **2021**, *93* (44), 14651-14658.

(46) Georgiou, R.; Gueriau, P.; Sahle, C. J.; Bernard, S.; Mirone, A.; Garrouste, R.; Bergmann, U.; Rueff, J.-P.; Bertrand, L. Carbon speciation in organic fossils using 2D to 3D x-ray Raman multispectral imaging. *Science Advances* **2019**, *5* (8), eaaw5019.

(47) Ngene, P.; Adelhelm, P.; Beale, A. M.; de Jong, K. P.; de Jongh, P. E. LiBH4/SBA-15 nanocomposites prepared by melt infiltration under hydrogen pressure: synthesis and hydrogen sorption properties. *The Journal of Physical Chemistry C* **2010**, *114* (13), 6163-6168.

(48) Barrett, E. P.; Joyner, L. G.; Halenda, P. P. The determination of pore volume and area distributions in porous substances. I. Computations from nitrogen isotherms. *Journal of the American Chemical society* **1951**, *73* (1), 373-380.

(49) Brunauer, S.; Emmett, P. H.; Teller, E. Adsorption of gases in multimolecular layers. *Journal of the American chemical society* **1938**, *60* (2), 309-319.

(50) Huotari, S.; Sahle, C. J.; Henriquet, C.; Al-Zein, A.; Martel, K.; Simonelli, L.; Verbeni, R.; Gonzalez, H.; Lagier, M.-C.; Ponchut, C. A large-solid-angle X-ray Raman scattering spectrometer at ID20 of the European Synchrotron Radiation Facility. *Journal of synchrotron radiation* **2017**, *24* (2), 521-530.

(51) Johnson, D. L. Local field effects and the dielectric response matrix of insulators: A model. *Physical Review B* **1974**, *9* (10), 4475.

(52) Sahle, C. J.; Mirone, A.; Niskanen, J.; Inkinen, J.; Krisch, M.; Huotari, S. Planning, performing and analyzing X-ray Raman scattering experiments. *Journal of synchrotron radiation* **2015**, *22* (2), 400-409.

(53) Blanchard, D.; Nale, A.; Sveinbjörnsson, D.; Eggenhuisen, T. M.; Verkuijlen, M. H. W.; Suwarno; Vegge, T.; Kentgens, A. P. M.; de Jongh, P. E. Nanoconfined LiBH4 as a Fast Lithium Ion Conductor. *Advanced Functional Materials* **2015**, *25* (2), 184-192. DOI: 10.1002/adfm.201402538.

(54) Suwarno, S.; Ngene, P.; Nale, A.; Eggenhuisen, T. M.; Oschatz, M.; Embs, J. P.; Remhof, A.; de Jongh, P. E. Confinement Effects for Lithium Borohydride: Comparing Silica and Carbon Scaffolds. *The Journal of Physical Chemistry C* **2017**, *121* (8), 4197-4205. DOI: 10.1021/acs.jpcc.6b13094.

(55) Lee, S. K.; Eng, P. J.; Mao, H.-k.; Meng, Y.; Shu, J. Structure of alkali borate glasses at high pressure: B and Li K-edge inelastic X-ray scattering study. *Physical review letters* **2007**, *98* (10), 105502.

(56) Pascal, T. A.; Boesenberg, U.; Kostecki, R.; Richardson, T. J.; Weng, T.-C.; Sokaras, D.; Nordlund, D.; McDermott, E.; Moewes, A.; Cabana, J. Finite temperature effects on the X-ray absorption spectra of lithium compounds: First-principles interpretation of X-ray Raman measurements. *The Journal of Chemical Physics* **2014**, *140* (3).

(57) Tsuji, J.; Nakamatsu, H.; Mukoyama, T.; Kojima, K.; Ikeda, S.; Taniguchi, K. Lithium K-edge XANES spectra for lithium compounds. *X-Ray Spectrometry: An International Journal* **2002**, *31* (4), 319-326.

(58) Wang, D.; Zuin, L. Li K-edge X-ray absorption near edge structure spectra for a library of lithium compounds applied in lithium batteries. *Journal of Power Sources* **2017**, *337*, 100-109.

(59) Hallmeier, K. H.; Szargan, R.; Meisel, A.; Hartmann, E.; Gluskin, E. S. Investigation of core-excited quantum yield spectra of high-symmetric boron compounds. *Spectrochimica Acta Part A: Molecular Spectroscopy* **1981**, *37* (12), 1049-1053. DOI: https://doi.org/10.1016/0584-8539(81)80148-1.

(60) Fleet, M.; Liu, X. Boron K-edge XANES of boron oxides: tetrahedral B–O distances and near-surface alteration. *Physics and Chemistry of Minerals* **2001**, *28*, 421-427.

(61) Fleet, M.; Muthupari, S. Coordination of boron in alkali borosilicate glasses using XANES. *Journal of non-crystalline solids* **1999**, *255* (2-3), 233-241.

(62) Fleet, M. E.; Muthupari, S. Boron K-edge XANES of borate and borosilicate minerals. *American Mineralogist* **2000**, *85* (7-8), 1009-1021.

(63) Yumatov, V.; Il'inchik, E.; Mazalov, L.; Volkov, O.; Volkov, V. X-ray and X-ray photoelectron spectroscopy studies of the electronic structure of borane derivatives. *Journal of Structural Chemistry* **2001**, *42*, 281-295.

(64) Qiao, R.; Chuang, Y.-D.; Yan, S.; Yang, W. Soft x-ray irradiation effects of Li2O2, Li2CO3 and Li2O revealed by absorption spectroscopy. *PloS one* **2012**, *7* (11), e49182.

(65) Yang, S.; Wang, D.; Liang, G.; Yiu, Y. M.; Wang, J.; Liu, L.; Sun, X.; Sham, T.-K. Soft X-ray XANES studies of various phases related to LiFePO 4 based cathode materials. *Energy & Environmental Science* **2012**, *5* (5), 7007-7016.

(66) Zhuravlev, L. The surface chemistry of amorphous silica. Zhuravlev model. *Colloids and Surfaces A: Physicochemical and Engineering Aspects* **2000**, *173* (1-3), 1-38.

(67) Choi, Y. S.; Lee, Y.-S.; Oh, K. H.; Cho, Y. W. Interface-enhanced Li ion conduction in a LiBH 4–SiO 2 solid electrolyte. *Physical Chemistry Chemical Physics* **2016**, *18* (32), 22540-22547.

(68) Matsuo, M.; Nakamori, Y.; Orimo, S.-i.; Maekawa, H.; Takamura, H. Lithium superionic conduction in lithium borohydride accompanied by structural transition. *Applied Physics Letters* **2007**, *91* (22).

(69) Neuville, D. R.; Cormier, L.; Flank, A.-M.; Prado, R. J.; Lagarde, P. Na K-edge XANES spectra of minerals and glasses. *European journal of mineralogy* **2004**, *16* (5), 809-816.

(70) Teodorescu, C.; El Afif, A.; Esteva, J.; Karnatak, R. Na 1 s excitations in vapor and solid sodium halides. *Physical Review B* **2001**, *63* (23), 233106.

(71) Niwa, M.; Katada, N.; Sawa, M.; Murakami, Y. Temperature-programmed desorption of ammonia with readsorption based on the derived theoretical equation. *The Journal of Physical Chemistry* **1995**, *99* (21), 8812-8816.

(72) Datka, J.; Góra-Marek, K. IR studies of the formation of ammonia dimers in zeolites TON. *Catalysis today* **2006**, *114* (2-3), 205-210.

(73) Busca, G. Spectroscopic characterization of the acid properties of metal oxide catalysts. *Catalysis Today* **1998**, *41* (1), 191-206. DOI: https://doi.org/10.1016/S0920-5861(98)00049-2.

(74) Velthoen, M. E.; Nab, S.; Weckhuysen, B. M. Probing acid sites in solid catalysts with pyridine UV-Vis spectroscopy. *Physical Chemistry Chemical Physics* **2018**, *20* (33), 21647-21659.

(75) Chorkendorff, I.; Niemantsverdriet, J. W. *Concepts of modern catalysis and kinetics*; John Wiley & Sons, 2017.

(76) Baca, M.; de La Rochefoucauld, E.; Ambroise, E.; Krafft, J.-M.; Hajjar, R.; Man, P. P.; Carrier, X.; Blanchard, J. Characterization of mesoporous alumina prepared by surface alumination of SBA-15. *Microporous and mesoporous materials* **2008**, *110* (2-3), 232-241.

(77) Klimova, T.; Peña, L.; Lizama, L.; Salcedo, C.; Gutiérrez, O. Y. Modification of activity and selectivity of NiMo/SBA-15 HDS catalysts by grafting of different metal oxides on the support surface. *Industrial & Engineering Chemistry Research* **2009**, *48* (3), 1126-1133.

(78) Ryoo, R.; Kim, M. J. Generalised route to the preparation of mesoporous metallosilicates via post-synthetic metal implantation. *Chemical Communications* **1997**, (22), 2225-2226.